JTTEE5 23:140–146
DOI: 10.1007/s11666-013-0026-5
1059-9630/$19.00 © ASM International

MCrAlY Bondcoats by High-Velocity Atmospheric Plasma Spraying

G. Mauer, D. Sebold, and R. Vaßen

(Submitted May 24, 2013; in revised form August 5, 2013)

MCrAlY bondcoats (M = Co, Ni) are used to protect metallic substrates from oxidation and to improve adhesion of ceramic thermal barrier coatings for high temperature applications, such as in land-based and aviation turbines. Since MCrAlYs are prone to take up oxygen during thermal spraying, bondcoats often are manufactured under inert gas conditions at low pressure. Plasma spraying at atmospheric conditions is a cost-effective alternative if it would be possible to limit the oxygen uptake as well as to obtain sufficiently dense microstructures. In the present work, high-velocity spray parameters were developed for the TriplexPro 210 three-cathode plasma torch using MCrAlY powders of different particle size fractions to achieve these objectives. The aims are conflictive since the former requires cold conditions, whereas the latter is obtained by more elevated particle temperatures. High particle velocities can solve this divergence as they imply shorter time for oxidation during flight and contribute to coating densification by kinetic rather than thermal energy. Further aims of the experimental work were high deposition efficiencies as well as sufficient surface roughness. The oxidation behavior of the sprayed coatings was characterized by thermal gravimetric analyses and isothermal heat treatments.

Keywords atmospheric plasma spraying, bondcoat, MCrAlY, thermal barrier coating, Triplex torch

1. Introduction

MCrAlY-type bondcoats (M = Co, Ni) are commonly used to protect metallic substrates from oxidation and to improve adhesion of ceramic thermal barrier coatings (TBCs) for high temperature applications such as in land-based and aviation gas turbines. During service an alumina-based oxide scale (thermally grown oxide, TGO) is formed at the bondcoat/topcoat interface. A dense TGO can prevent oxygen from diffusing into the bondcoat so that metallic substrates are protected from rapid high temperature oxidation attack. The lifetime of the TBCs is associated with the formation of such TGO, whereby the failure frequently occurs at the scale/metal interface (Ref 1). Thus, the oxidation behavior of MCrAlY-type bondcoats is of importance. Besides the MCrAlY composition (major elements Co, Ni, and Cr as well as minor additions such as Y, La, Hf, Zr, Ca, Si, etc.) (Ref 2, 3), atmosphere composition (Ref 4), exposure conditions (Ref 5), surface conditions (Ref 6), and the manufacturing related parameters (thickness, microstructure, oxygen content, etc.) strongly affect the bondcoat performance (Ref 7-9).

Since MCrAlYs are prone to take up oxygen during thermal spraying, bondcoats are often manufactured under inert gas conditions at low pressure (low pressure plasma spraying, LPPS, earlier called vacuum plasma spraying, VPS) (Ref 10). This however is expensive. Plasma spraying at atmospheric conditions (APS) is an appropriate alternative if it would be possible to limit the oxygen uptake as well as to obtain dense microstructures with sufficient surface roughness. The newly developed TriplexPro-210 three-cathode plasma torch (Ref 11, 12) gives interesting opportunities to such approach as it enables high plasma gas flows and the use of high-velocity nozzles with small diameters. This results in lower plume temperatures and higher particle velocities so that the conditions can come closer to those of high-velocity oxy-fuel (HVOF) spraying. However, the spray distance (SD) is distinctly smaller and if the particle velocities are sufficient the dwell times can be shorter than in HVOF. Furthermore, APS does not use oxygen as a process gas. Considered together, this should be advantageous regarding low oxygen take-up during spraying. Another alternative is the new cold spray (CS) process since gas temperatures and pressures can be adjusted far enough to deposit solid metallic alloys with higher strength such as MCrAlYs. Cold sprayed bond coats were obtained with low oxygen contents compared to specimens manufactured by LPPS (Ref 13). The porosities were reported to be similar and TGOs were homogeneous with respect to their thickness and composition (Ref 14). Hence, cold spraying might be an appropriate candidate. Besides technological features, also economic aspects have to be considered to evaluate the competitiveness of APS and CS processes.

This article is an invited paper selected from presentations at the 2013 International Thermal Spray Conference, held May 13-15, 2013, in Busan, South Korea, and has been expanded from the original presentation.

G. Mauer, D. Sebold, and **R. Vaßen**, Institut für Energie- und Klimaforschung (IEK-1), Forschungszentrum Jülich, Jülich, Germany. Contact e-mail: g.mauer@fz-juelich.de.

In the present work, high-velocity APS spray parameters for MCrAlY bondcoats were developed using the TriplexPro-210 torch to achieve the objectives of low oxygen content and porosity. These objectives are conflicting since the former requires cold conditions, whereas the latter is supported by more elevated particle temperatures. High particle velocities can solve this divergence as they imply shorter time for oxidation during flight and contribute to coating densification by kinetic rather than thermal energy. Further objectives of the experimental work were high deposition efficiencies as well as sufficient surface roughness (according to the author's experience $R_a > 6$ µm). The oxidation behavior of the sprayed coatings was characterized by thermal gravimetric analyses and isothermal heat treatments.

2. Experimental Procedures

The experiments were performed by atmospheric plasma spraying in a MultiCoat™ facility with a three-cathode TriplexPro™-210 torch (both by Sulzer Metco, Wohlen, Switzerland) mounted on a six-axis robot. The diameter of the applied high-speed nozzle was 5 mm; the injector diameter was 1.8 mm with an angle of 90° relative to the torch axis. The current was 450 A which is the highest applicable with the 5-mm nozzle, according to the torch specifications. Further spray parameters are given in Table 1. Higher plasma gas flow than 190 slpm Ar plus 40 slpm He was not available due to limitations of the spray facility and gas supply. Estimating the plasma gas temperature to be approximately 10,000 K at atmospheric pressure, see below, these conditions are distinctly supersonic at Mach numbers ≈4. Hence, the plasma jet showed pronounced shock diamonds indicating the shock fronts between successive expansion and compression cells.

The feedstock was a commercially available gas-atomized powder (Sulzer Metco Amdry 9951-F) with a spherical morphology ($d_{10} = 12$ µm, $d_{50} = 18$ µm, $d_{90} = 26$ µm, measured by laser diffraction). The feed rate was 40 g/min. Coatings obtained in initial tests with coarser powder fractions Amdry 9951 ($d_{10} = 15$ µm, $d_{50} = 25$ µm, $d_{90} = 38$ µm) and Amdry 9954 ($d_{10} = 17$ µm, $d_{50} = 29$ µm, $d_{90} = 47$ µm) showed too large porosities and smaller deposition efficiencies. The nominal composition of Amdry 995x powders is Co-32Ni-21Cr-8Al-0.5Y (by wt.%). The initial oxygen content of the Amdry 9951-F used in this work was 495 ppm (determined by chemical analysis). The SDs were varied at 80, 100, and 120 mm.

Table 1 Applied spray parameters

Parameter	A	B
Primary plasma gas flow, slpm Ar	190	190
Secondary plasma gas flow, slpm He	20	40
Torch input power, kW	70.4	73.6
Carrier gas flow, slpm Ar	6.0	6.5
Spray distance, mm	100	100

slpm, standard liters per minute

The raster speed was 500 mm/s, the meander spacing 2 mm, and the number of passes 5. Figure 1 shows the optimization of the carrier gas flows by identification of maximum deposition efficiencies (DE) which were determined from the coating masses and the powder mass feed rate. Table 1 shows the optimized carrier gas flows.

The coatings were sprayed onto Inconel 738 LC substrates. Some specimens were subjected to a two-stage vacuum annealing (2 h at 1120 °C and 24 h at 845 °C) for diffusion bonding and homogenization. Microstructures were analyzed by scanning electronic microscopy with energy dispersed spectroscopy (EDX), oxide content and porosity by digital image analyses and phases by x-ray diffraction (XRD).

3. Results and Discussion

3.1 As-Sprayed Microstructures

Figure 2 gives an overview of the as-sprayed coating microstructures obtained by parameters A and B at SD 100 mm. Figure 3 shows some details at larger magnification. In particular, for parameter B, it is evident that many of the gaps between the larger less deformed particles are well filled by smaller strongly distorted splats. The arithmetic mean surface roughness for both samples is similar at $R_a \approx 7$ µm. The trend decreases slightly with increasing SD (see Fig. 4). Obviously, the splats are a bit more fragmented at smaller SDs due to their larger kinetic energy. DE is slightly higher for parameter B (61%) than for parameter A (58%); this difference is significant. The DEs were found to be maximum at SD 100 mm in both cases and decreased for shorter as well for longer SDs. This maximum might be a result of two effects. At shorter SD, particles are more fragmented and may partly tend to bounce off; at longer SD, the deposition is less efficient due to the smaller kinetic energy.

Figure 5 shows the formation of oxides in the as-sprayed coating microstructure obtained by parameter B at SD 80 mm. The feedstock particles are still identifiable, also some porosity and voids as the particle deformation was not sufficient to fill all the gaps between them. Furthermore, thin oxide scales are discernible on the splat

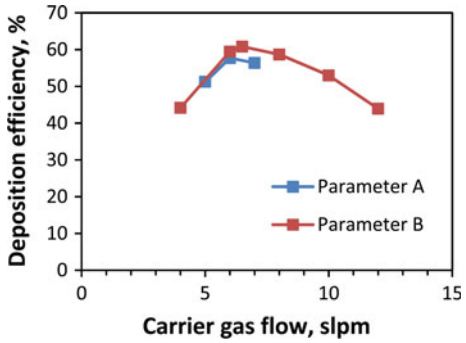

Fig. 1 Optimization of carrier gas flows for spray parameters A and B on the basis of deposition efficiencies at SD 100 mm

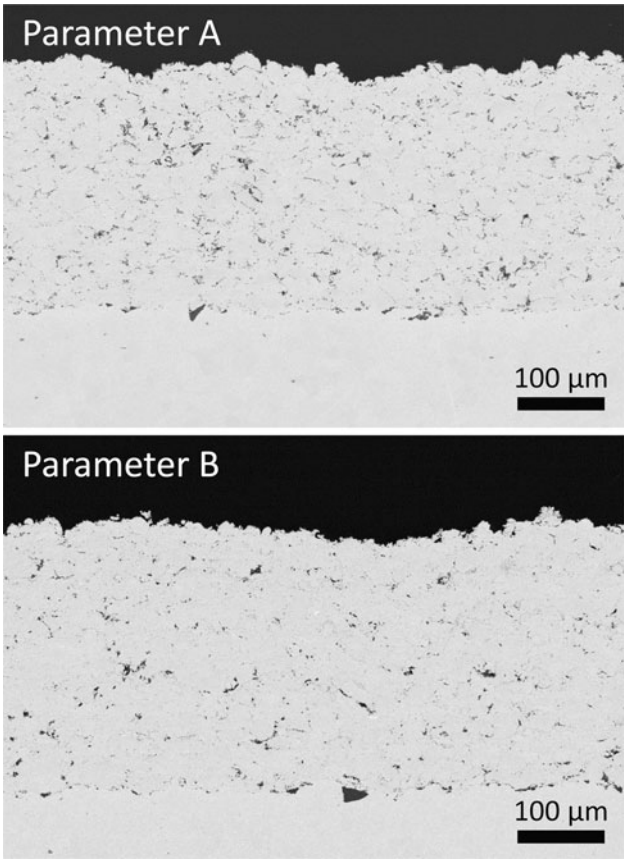

Fig. 2 Overview of as-sprayed coating microstructures obtained by parameters A and B at SD 100 mm (back-scattered electron images)

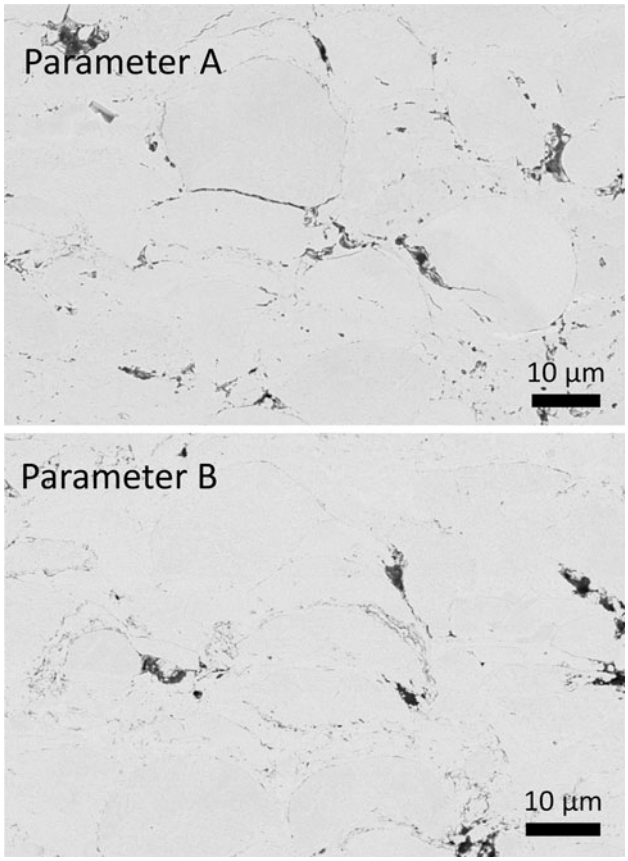

Fig. 3 Details of as-sprayed coating microstructures obtained by parameters A and B at SD 100 mm (back-scattered electron images)

boundaries due to in-flight oxidation. With smaller SDs, more of such oxides are found on top of the layers deposited at each pass. Thus, oxidation of the hot coating surface immediately after deposition of each pass is assumed.

Porosity and oxides were analyzed and quantified by digital image analysis; particular gray scale ranges were attributed to porosity and oxides, respectively. For each data point, the results of three frames were averaged and are given in Fig. 6; the error bars refer to the individual standard deviations. The porosity is quite low at comparable magnitude to LPPS coatings (is below 3% according to the author's standard process; parameters can be found elsewhere, Ref 10). It is on the same level for the parameter B with high helium content, while it increases for the low helium parameter A with increasing SD. In the latter case, one reason might be that the particles were already cooling down in-flight so that larger porosity was formed. The high helium content of parameter B implies hotter conditions since generally more oxide was formed compared to parameter A (bottom chart of Fig. 6).

The oxygen content was determined also quantitatively by chemical analysis. The result for the sample sprayed with parameter B at SD 100 mm was 0.41 ± 0.04 wt.% oxygen. This is more than in LPPS coatings exhibiting

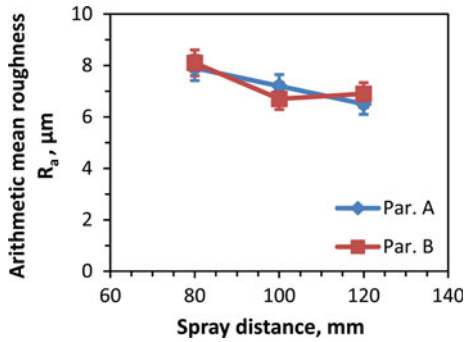

Fig. 4 Arithmetic mean surface roughness obtained by parameters A and B at different SDs (stylus profilometry)

typical oxygen contents below 0.1 wt.% (Ref 10). However, it is considerably lower than found in conventional APS bondcoats (Ref 15) and also lower than that often observed in HVOF sprayed coatings (Ref 16). Here, the oxygen take-up during flight can be substantially higher and depends significantly on the feedstock particle size and SD (Ref 17). By HVOF, lower oxygen contents than 0.4 wt.% could only be achieved with coarser powders which on the other hand make it difficult to obtain low porosities (Ref 18).

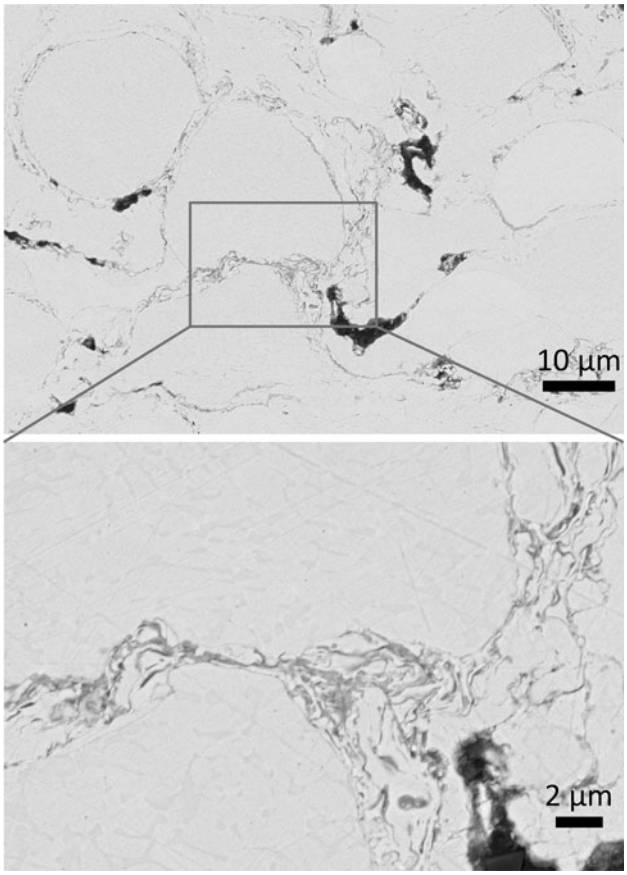

Fig. 5 Oxide formation in as-sprayed coating microstructures obtained by parameter B at SD 80 mm (back-scattered electron images)

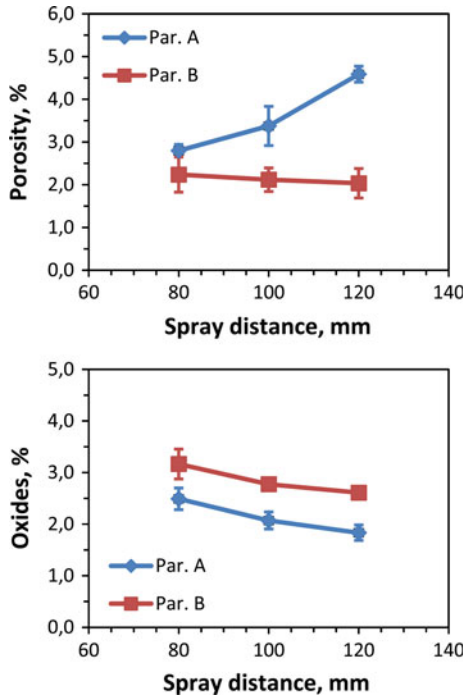

Fig. 6 Oxide content and porosity determined by digital image analysis of back-scattered electron images (expressed by percentages of area in cross-sectional images)

Table 2 Estimated plasma gas transport properties

Parameter	A	B
Torch net power, kW	38.7	39.5
Dynamic viscosity, 10^{-4} Pa/s	2.66	2.69
Thermal conductivity, W/m·K	0.98	1.04

Porosity and oxidation are highly dependent on the particle in-flight characteristics. To assess the influence of the plasma gas composition on particle acceleration and heating, the transport properties for momentum and heat transfer have to be considered. As they are temperature dependent, the plasma gas temperature needs to be estimated first. For both the plasma gas compositions of parameters A and B, enthalpy flows are calculated for various temperatures using tabulated specific-enthalpy data of the constituent elements (Ref 19). The torch net power is assumed to be the enthalpy flow into the plasma. Matching these enthalpy flows leads to the plasma gas temperature at the nozzle exit of the torch. As they are around 10,000 K for both parameters A and B, the conditions are quite cold compared to usual APS processes (Ref 20).

Using this temperature, the transport properties were calculated by means of the CEA code (Ref 21) assuming atmospheric pressure and thermodynamic equilibrium. The results are listed in Table 2. The dynamic viscosity is almost the same for both parameters as these are below the first ionization temperatures of Ar and He, respectively, and are associated with a distinct drop of the viscosities. This means that particle acceleration is very similar in both cases because the drag force which is exerted by the plasma gas flow on the particles is directly proportional to the dynamic viscosity at the first approximation (Stokes solution for the flow around a sphere, Ref 20).

The heat flow from the plasma gas to the particles is proportional to the convective heat transfer coefficient which on the other hand is proportional to the Nusselt number and the thermal conductivity of the plasma gas. The Nusselt number is a function of the Reynolds and the Prandtl numbers (Ref 22), which are similar for both parameters. However, the thermal conductivity is higher for parameter B containing more helium than parameter A. Thus, particle heating is more effective leading to smaller porosities due to the higher melting grade and viscosity of the molten splats as well as to some extent, more oxidation (Fig. 6). Unfortunately, the particle temperatures could not be verified by particle diagnostics since their thermal radiation was not sufficiently detectable due to the relatively cold conditions. But the maximum sample surface temperatures measured by pyrometer during spraying confirm that the conditions of parameter B are hotter (see Fig. 7). It must be noted that the quantitative results of such measurements are

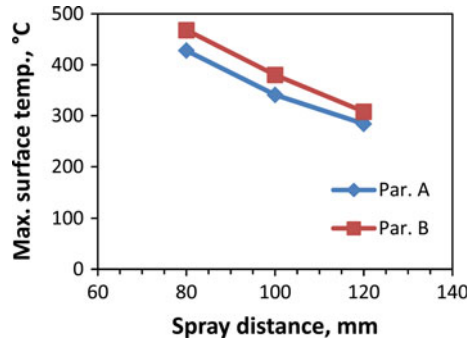

Fig. 7 Maximum surface temperatures measured by pyrometer during spraying for parameters A and B at different SDs

subjected to limited resolution with regard to time and measuring position.

3.2 As-Annealed Microstructures

After heat treatment only a few pores are left and the porosity decreases below 1% (determined by digital image analysis), as shown for a sample by parameter B at SD 100 mm in Fig. 8. On the surface of the initial feedstock particles, thin oxide layers containing mostly alumina (found by EDX) are spheroidized and form thin chains on the splat boundaries. This is not observed in such pronounced manner in LPPS coatings due to the lower oxidation. A closer look to the structure shows the distribution of body centered cubic β-phase (Co,Ni)Al and γ-phase (face-centered cubic (Co,Ni) solid solution including other elements like Cr and Al) as well as some needle-like γ′-phase $Al(Ni,Co)_3$. This, on the other hand, looks well-known also from LPPS coatings.

3.3 Crystallographic Results

The results of the XRD analysis of the as-sprayed as well as annealed coatings sprayed with parameter B using SD 100 mm are shown in Fig. 9. A vacuum-annealed reference coating manufactured by the author's LPPS standard process (parameters can be found elsewhere, Ref 10) is also given for comparison. While in the feedstock β-phase reflexes are evident, in the as-sprayed state mainly peaks of the γ-phase are visible. The γ-phase reflexes may represent also the γ′-phase which is hardly distinguishable. The fact that almost no β-phase can be identified (except for a small shoulder right to the main γ-peak) suggests that it is mostly dissolved into the γ-phase due to the intense plastic deformation during deposition as observed also in CS or HVOF sprayed coatings (Ref 23).

The Williamson-Hall plot method yields a crystallite size <10 nm and -1% compressive strain. Another reference sample sprayed by HVOF using the DJ2600 gun (Sulzer Metco, Wohlen, Switzerland, not shown in this paper) exhibited the same magnitude of crystallite sizes but with higher compressive strain of -2%. After two-stage vacuum-annealing for precipitation and homogenization treatment the peaks of the β-phase become

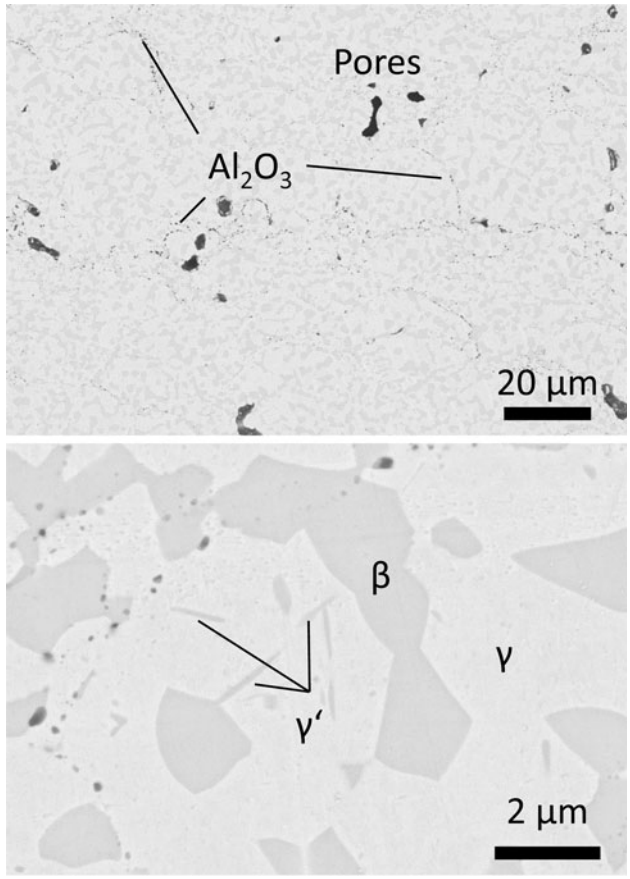

Fig. 8 Phase structure of a coating sprayed with parameter B at SD 100 mm as-annealed (back-scattered electron images)

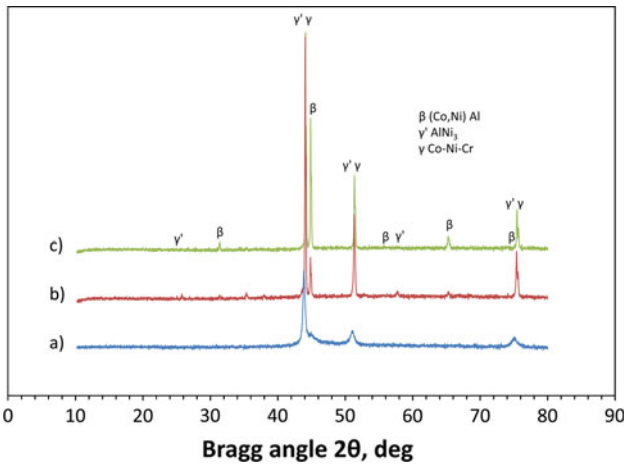

Fig. 9 XRD analysis of coatings sprayed with parameter B at SD 100 mm: (a) as-sprayed and (b) vacuum-annealed; (c) reference coating manufactured by LPPS, vacuum-annealed

prominent. The crystallite size is ≈240 nm and the strains have relaxed to 0.1%. These results are very similar to the annealed reference sample sprayed by LPPS (≈200 nm, strain 0%).

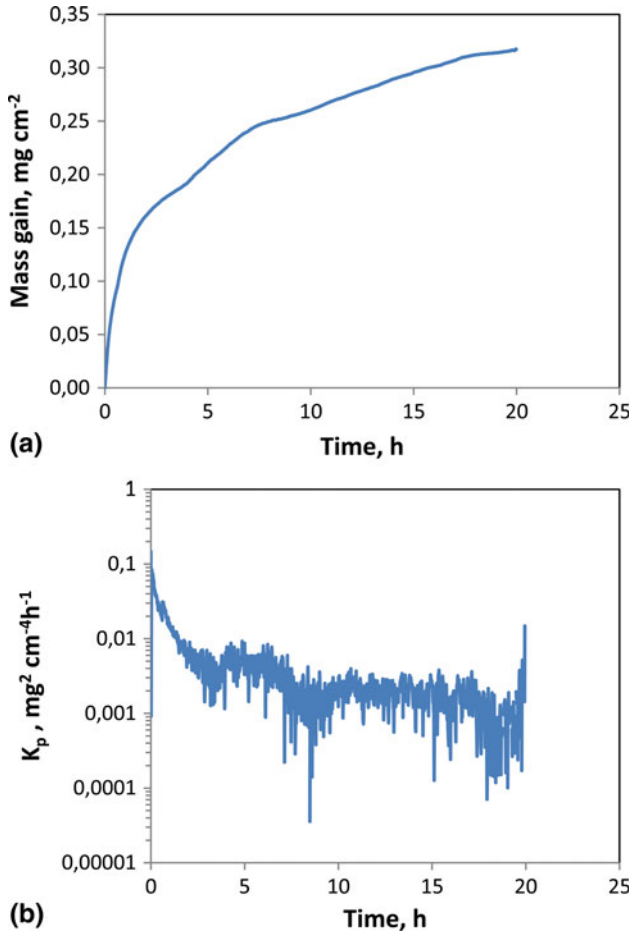

Fig. 10 Results of TGA at 1000 °C during 20 h in air of a vacuum annealed sample sprayed by parameter B at SD 100 mm: (a) mass gain related to sample surface and (b) instantaneous oxidation rate

3.4 Oxidation Behavior

To study the oxidation behavior, the oxygen take up of freestanding vacuum annealed bondcoat samples sprayed by parameter B at SD 100 mm was investigated at 1000 °C during 20 h in air by thermal gravimetric analysis (TGA). Figure 10(a) gives the mass gain related to the sample surface area. Figure 10(b) shows the instantaneous oxidation rate

$$k_p = \frac{d\left(\Delta m(t)^2\right)}{dt}, \qquad \text{(Eq 1)}$$

where k_p represents the parabolic oxidation rate, Δm the sample mass gain related to the sample surface area, and t the time. This is according to Wagner's theory of parabolic oxidation assuming that the rate determining step in the oxidation process is volume diffusion of reacting ions or corresponding defects through a compact oxide scale and that other diffusion paths, e.g., along grain boundaries can be neglected (Ref 24). This approach means that the thicker the oxide scale is at any point of time, the slower is the rate of subsequent oxidation. The determined mass gain and oxidation rate are well comparable to the TGA results for LPPS manufactured CoNiCrAlY coatings reported in Ref. 25. According to the same reference, the higher oxidation rate during the first 10 h exposure can be associated to the initial formation of meta-stable θ-alumina at 1000 °C. The oxidation rate decreases as this phase is transformed to α-alumina at longer times.

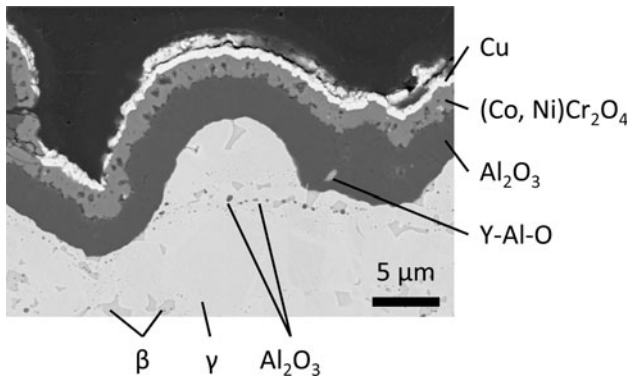

Fig. 11 Thermally grown oxide layer on the as-sprayed surface of an annealed coating sprayed with parameter B at SD 100 mm after 10-h exposure in air at 1100 °C and atmospheric pressure (back-scattered electron image)

Another freestanding annealed sample was oxidized at 1100 °C and atmospheric pressure for 10 h. Figure 11 shows the cross-section of the as-sprayed surface. The indicated phases were determined by EDX. Before cross-sectioning, the sample was coated with a thin Cu layer by electron beam PVD to protect the TGO. It consists of an outer porous $(Co,Ni)(Cr,Al)_2O_4$ spinel layer (~1.5 µm) and a dense inner-alumina layer (~2.5-3 µm). Fewer yttrium aluminates Y-Al-O are visible than typically observed in the TGO of LPPS bondcoats. This might be an indication that yttrium has been consumed by oxide formation inside the coating. Actually, the strings of small spheroidized oxides on the splat boundaries contain besides alumina obviously also yttrium aluminates (likely $Y_3Al_5O_{12}$) and possibly Yttria as the back-scattered electron images show different gray scales. Consequently, less metallic compounds with yttrium could form on the grain boundaries which are deemed to moderate the Al diffusion favorably. The coating structure below the surface shows the typical depletion of the β-phase due to aluminum diffusion into the TGO. However, some β-phase is still present.

4. Conclusions

Atmospheric plasma spray parameters were developed for the use of TriplexPro-210 plasma torch with a high-velocity nozzle in order to deposit MCrAlY bondcoats. Initial experiments yielded the best results regarding the coating microstructure using a fine powder with a median particle size of 18 µm. Although the spray conditions were relatively cold, reasonable deposition efficiencies and rather dense coatings could be achieved. The comparison

of two plasma gas compositions showed that helium promotes particle heating leading to the lowest porosities almost comparable to LPPS coatings and better than typically obtained by HVOF.

In principle, the oxygen content is similar to good HVOF sprayed coatings; however, not as low as usually achieved by LPPS. Nevertheless, the oxidation protection of these bondcoats should be sufficient for many applications which are subjected to restricted temperatures. The oxidation behavior seems to be without peculiarities. One distinctive feature compared to LPPS bondcoats, is the formation of small oxide strings on the splat boundaries obviously consuming yttrium. Providing a feedstock with higher yttrium content may be an option to prevent a deficit of reactive elements.

Acknowledgments

The authors gratefully acknowledge the cooperation of Dr. A. Barth, Dr. M. Gindrat and Dr. H.-M. Höhle, all from Sulzer Metco. They also thank M.-T. Gerhards for the TG analyses, M. Kappertz for the metallographic preparation and F. Vondahlen for the EB-PVD coatings (all from Forschungszentrum Jülich, IEK-1).

References

1. D. Naumenko, V. Shemet, L. Singheiser, and W.J. Quadakkers, Failure Mechanisms of Thermal Barrier Coatings on MCrAlY-Type Bondcoats Associated with the Formation of the Thermally Grown Oxide, *J. Mater. Sci.*, 2009, **44**, p 1687-1703
2. J. Toscano, R. Vaßen, A. Gil, M. Subanovic, D. Naumenko, L. Singheiser, and W.J. Quadakkers, Parameters Affecting TGO Growth and Adherence on MCrAlY-Bond Coats for TBCs, *Surf. Coat. Technol.*, 2006, **201**, p 3906-3910
3. A. Gil, D. Naumenko, R. Vaßen, J. Toscano, M. Subanovic, L. Singheiser, and W.J. Quadakkers, Y-Rich Oxide Distribution in Plasma Sprayed MCrAlY-Coatings Studied by SEM with a Cathodoluminescence Detector and Raman Spectroscopy, *Surf. Coat. Technol.*, 2009, **204**, p 531-538
4. P. Song, M. Subanovic, J. Toscano, D. Naumenco, and W.J. Quadakkers, Effect of Atmosphere Composition on the Oxidation Behavior of MCrAlY Coatings, *Mater. Corros.*, 2011, **62**(7), p 699-705
5. M. Subanovic, P. Song, R. Vaßen, D. Naumenko, L. Singheiser, and W.J. Quadakkers, Effect of Exposure Conditions on the Oxidation of MCrAlY-Bondcoats and Lifetime of Thermal Barrier Coatings, *Surf. Coat. Technol.*, 2009, **204**, p 820-823
6. A. Gil, V. Shemet, R. Vaßen, M. Subanovic, J. Toscano, D. Naumenko, L. Singheiser, and W.J. Quadakkers, Effect of Surface Condition on the Oxidation Behavior of MCrAlY Coatings, *Surf. Coat. Technol.*, 2006, **201**, p 3824-3828
7. M. Subanovic, D. Sebold, R. Vaßen, E. Wessel, D. Naumenko, L. Singheiser, and W.J. Quadakkers, Effect of Manufacturing Related Parameters on Oxidation Properties of MCrAlY-Bondcoats, *Mater. Corros.*, 2008, **59**(6), p 463-470
8. W.R. Chen, X. Wu, B.R. Marple, D.R. Nagy, and P.C. Patnaik, TGO Growth Behavior in TBCs with APS and HVOF Bond Coats, *Surf. Coat. Technol.*, 2008, **202**, p 2677-2683
9. M. Di Fernandino, A. Fossati, A. Lavacchi, U. Bardi, F. Borgioli, C. Borri, C. Giolli, and A. Scrivani, Isothermal Oxidation Resistance Comparison Between Air Plasma Sprayed, Vacuum Plasma Sprayed and High Velocity Oxygen Fuel Sprayed CoNiCrAlY Bond Coats, *Surf. Coat. Technol.*, 2010, **204**, p 2499-2503
10. G. Mauer, R. Vaßen, and D. Stöver, Controlling the Oxygen Contents in Vacuum Plasma Sprayed Metal Alloy Coatings, *Surf. Coat. Technol.*, 2007, **201**(8), p 4796-4799
11. G. Mauer, R. Vaßen, and D. Stöver, Preliminary Study of the Triplexpro™-200 Gun for Atmospheric Plasma Spraying of Yttria-Stabilized Zirconia, *Surf. Coat. Technol.*, 2008, **202**(18), p 4374-4381
12. K. Landes, Plasma Generators for Thermal Plasma Processes, *Int. J. Mater. Res.*, 2011, **102**(8), p 959-963
13. A. Manap, A. Nakano, and K. Ogawa, The Protectiveness of Thermally Grown Oxides on Cold Sprayed CoNiCrAlY Bond Coat in Thermal Barrier Coating, *J. Therm. Spray Technol.*, 2012, **21**(3-4), p 569-586
14. Y. Li, C.-J. Li, G.-J. Yang, and L.-K. Xing, Thermal Fatigue Behavior of Thermal Barrier Coatings with the MCrAlY Bond Coats by Cold Spraying and Low-Pressure Plasma Spraying, *Surf. Coat. Technol.*, 2010, **205**, p 2225-2233
15. T. Patterson, A. Leon, B. Jayaraj, J. Liu, and Y.H. Sohn, Thermal Cyclic Lifetime and Oxidation Behavior of Air Plasma Sprayed CoNiCrAlY Bond Coats for Thermal Barrier Coatings, *Surf. Coat. Technol.*, 2008, **203**, p 437-441
16. M. Shibata, S. Kuroda, H. Murakami, M. Ode, M. Watanabe, and Y. Sakamoto, Comparison of Microstructure and Oxidation Behavior of CoNiCrAlY Bond Coatings Prepared by Different Thermal Spray Processes, *Mater. Trans.*, 2006, **47**(7), p 1638-1642
17. D. Seo, K. Ogawa, T. Shoji, and S. Murata, Effect of Particle Size Distribution on Isothermal Oxidation Characteristics of Plasma Sprayed CoNi- and CoCrAlY Coatings, *J. Therm. Spray Technol.*, 2007, **16**(5-6), p 954-966
18. B. Rajasekaran, G. Mauer, and R. Vaßen, Enhanced Characteristics of HVOF Sprayed MCrAlY Bond Coats for TBC Applications, *J. Therm. Spray Technol.*, 2011, **20**(6), p 1209-1216
19. M.W. Chase, Jr., NIST-JANAF Thermochemical Tables, 4th Ed., *J. Phys. Chem. Ref. Data*, 1998, Monograph 9
20. M. Vardelle, A. Vardelle, P. Fauchais, and M.I. Boulos, Plasma-Particle Momentum and Heat Transfer: Modelling and Measurements, *AIChE J.*, 1983, **29**(2), p 236-243
21. B. McBride and S. Gordon, *Chemical Equilibrium Program CEA2*, NASA Glenn Research Center, Cleveland, OH, 2004
22. R.M. Young and E. Pfender, Nusselt Numbers Correlations for Heat Transfer to Small Spheres in Thermal Plasma Flows, *Plasma Chem. Plasma Process.*, 1987, **7**(2), p 211-229
23. P. Richer, A. Zúñiga, M. Yandouzi, and B. Jodoin, CoNiCrAlY Microstructural Changes Induced During Cold Gas Dynamic Spraying, *Surf. Coat. Technol.*, 2008, **203**, p 364-371
24. *High-Temperature Oxidation-Resistant Coatings*, National Academy of Science/National Academy of Engineering, Washington, DC, 1970
25. J. Toscano, D. Naumenko, A. Gil, L. Singheiser, and W.J. Quadakkers, Parameters Affecting TGO Growth Rate and the Lifetime of TBC Systems with MCrAlY-Bondcoats, *Mater. Corros.*, 2008, **59**(6), p 501-507